Scientia Iranica B (2022) 29(6), 3017–3031

Sharif University of Technology
Scientia Iranica
Transactions B: Mechanical Engineering
http://scientiairanica.sharif.edu

Enhancement effect of multi-stage inducing duct on the wind velocity profile

M. Tahani[a,*], M. Masdari[a], A. Habibi[a], and M. Mirhosseini[b]

a. *Department of Aerospace Engineering, Faculty of New Sciences and Technologies, University of Tehran, Tehran, Iran.*
b. *School of Advanced Technologies, Iran University of Science and Technology, Tehran, Iran.*

Received 4 May 2021; received in revised form 18 January 2022; accepted 1 August 2022

KEYWORDS
Wind energy;
Multi-stage inducing duct;
Inducing suction effect;
Wind power augmentation;
Low-speed winds.

Abstract. To extract power from the wind, the high enough velocity of the wind is a key factor. However, winds with high enough velocities are not available in most areas; therefore, finding a method to enhance the velocity potential of the low-speed winds remains a serious challenge in wind engineering. In this study, a hollow duct with a specific configuration, called Multi-Stage Inducing Duct, is presented which is capable of significantly enhancing the velocity profile of low-speed winds, enough to start most of the small horizontal wind turbines. For example, a three-stage inducing duct can increase the wind velocity from 3 m/s to 9.3 m/s on average at the first-stage throat of the duct, which equals the increase rate of 29 times in wind potential power. This configuration of the duct was introduced and numerically simulated. Moreover, the effects of its different geometrical parameters were investigated. The impact of wind velocity and the number of the stages on the duct performance were investigated. Finally, a study of the relative effectiveness of adding each of the stages was carried out to help decide where the upper limit for the number of the stages is.

1. Introduction

For years, fossil fuels have been the main source of energy in the world. However, global warming and environmental pollutions caused by fossil fuels have forced scientists to think of finding some clean alternative energy sources. Wind as a green source of energy has received much attention in recent years, and most countries are planning to develop wind power plants. Wind turbines are the machines that extract mechanical power from the wind and they mainly of two types: Vertical Axis Wind Turbines (VAWTs) and Horizontal Axis Wind Turbines (HAWTs). Tahani et al. (2016) studied a straight blade VAWT using Double Multiple Stream Tube (DMST) theory. First, a DMST code was developed and validated based on existing experimental results. Then, the VAWT design was optimized using a novel heuristic method presented in [1]. Tahani et al. (2017) designed and numerically investigated a Savonius VAWT with discharge flow directing capability. They modified the design of the turbine and demonstrated that using a twisted Savonius wind turbine with a conical shaft would improve the power coefficient by 18% compared to a simple Savonius wind turbine [2]. Tahani et al. (2017) investigated the effect of geometrical parameters on the performance of a HAWT at different turbulence intensities using the theory of Blade Element Momentum (BEM). Then, the results of the BEM algorithm were validated using existing experimental data and the shape of the blades was optimized using the popular ant colony optimization algorithm. They found that optimization of the geometry caused

*. *Corresponding author.*
E-mail address: m.tahani@ut.ac.ir (M. Tahani)

doi: 10.24200/sci.2022.58219.5639

a delay in the flow separation and therefore, more power could be extracted [3]. Tahani et al. (2017) aerodynamically designed and optimized a 1 mega-Watt HAWT based on BEM. Using a new linearization method, they considered linear distributions for chord lengths and twist angles of the blade cross-sections, and the optimum linearized distributions were obtained considering the power coefficient as the optimization criterion [4]. Finding a solution to extract power from the wind, despite its stochastic nature, helps use this source of energy in many situations where the wind does not blow at high enough velocity and throughout enough hours of the day. Use of hybrid methods is a way to extract power from the wind even though it does not blow sufficiently during the day. In 2015, Tahani et al. optimized a hybrid system for a three-story building in Tehran, Iran [5]. In case of low-velocity wind, the use of a duct is an old solution to increase the wind velocity enough to ensure an economical power generation. Duct augmentation to enhance the power generated by a wind turbine remains the subject of various researches. Abe et al. (2005) carried out both experimental and numerical investigations of the flow field of a small wind turbine with a flanged diffuser [6]. Ohya et al. (2008) experimentally investigated the effects of various geometrical characteristics of a flanged diffuser on the performance of a flange-ducted wind turbine. They reported a power augmentation of 4-5 compared to the bare turbine [7]. Kosasih and Tondelli (2012) experimentally investigated a micro-ducted wind turbine. They studied the effects of the shape and geometrical features of the shroud [8]. Jafari and Kosasih (2014) numerically simulated a small wind turbine equipped with a simple frustum diffuser [9]. Mansour and Meskinkhoda (2014) investigated flow fields around flanged diffusers using computational fluid dynamics [10]. In recent years, some researchers have developed new ideas to extract power from low-speed winds. Zabihzadeh et al. (2015) suggested adding a step inside the diffuser to cause separation and achieve more suction due to the low-pressure region caused by the separation [11]. Han et al. (2015) introduced a new duct that was able to increase the wind velocity effectively and extract power from the low-speed winds [12]. Al-Sulaiman (2017) brought up the idea of putting an ejector at the outlet of the wind turbine duct to increase the duct suction [13]. Khamlaj and Rumpfkeil (2018) computationally investigated a flanged diffuser-augmented wind turbine using open-source code software OpenFOAM [14]. Saleem and Kim (2019) studied the effect of rotor tip clearance on the aerodynamic performance of an airfoil-based ducted wind turbine [15]. Noorollahi et al. (2020) carried out a numerical investigation into the flow around a small ducted wind turbine [16]. Keramat et al. (2020) presented the idea of using a variable and controllable nozzle-diffuser duct with a wind turbine [17]. Bontempo and Manna (2020) conducted a review and assessment of the most important theoretical models conceived for the performance analysis and design of the diffuser augmented wind turbines [18]. Keramat et al. (2020) presented a mathematical model of a shrouded wind turbine and demonstrated that the power coefficient of 0.93 could be reached using a properly designed duct [19]. Prasad et al. (2020) computationally studied three types of diffuser ducts: straight ducts, curved ducts, and Vortex Generators (VGs) ducts. They also studied the effect of brimmed ducts and reported an improvement in power particularly about curved ducts and VGs ducts [20]. Rivarolo et al. (2020) studied the effect of Yaw angle on the performance of a convergent-divergent ducted wind turbine [21]. Avallone et al. (2020) delved into the effect of the tip-clearance ratio on the aeroacoustics of a diffuser-augmented wind turbine [22]. Nardecchia et al. (2021) analyzed a mini ducted wind turbine utilizing numerical simulation. They compared the results with those of a similar turbine installed in the open field and reported an increase of up to 432% in the extracted energy thanks to the use of the duct [23].

In this research study, a specific duct configuration for horizontal wind turbines is introduced that can provide a great augmentation in wind velocity profile compared to other presented ducts. This configuration, called "Multi-Stage Inducing Duct", is shown in Figure 1. In this configuration, each downstream stage strengthens the suction produced by its upstream stage; finally, the maximum suction occurs at the first-stage throat, where the wind turbine should be placed there.

All stages are supposed to be cast of aluminum due to its lightness, acceptable strength, and stainless properties. A value of 4 mm is assigned to the body thickness of all the stages. At the two ends of all stages

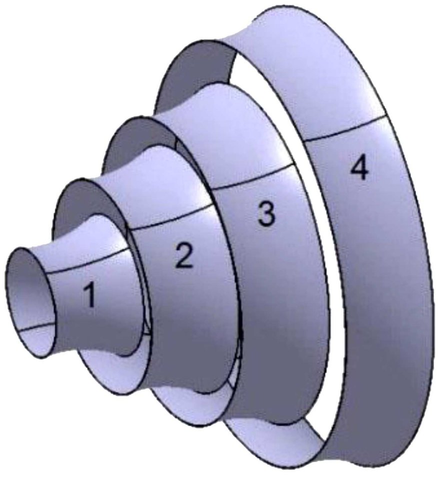

Figure 1. Configuration of the multi-stage inducing duct.

(at the inlet of nozzles and the outlet of diffusers), edges are designed to be rounded (circular).

2. Numerical method

2.1. Governing equations

The general form of the continuity and momentum conservation equations is as follows:

$$\frac{\partial \rho}{\partial t} + \frac{\partial}{\partial x_i}(\rho u_i) = 0, \quad (1)$$

$$\frac{\partial}{\partial t}(\rho u_i) + \frac{\partial}{\partial x_j}(\rho u_i u_j) = -\frac{\partial P}{\partial x_i} + \frac{\partial \tau_{ij}}{\partial x_j} + \rho g_i + F_i, \quad (2)$$

where ρ is the fluid density; x_i and u_i are the length and velocity components in the ith spatial direction, respectively. P is the static pressure; g_i and F_i represent the gravitational acceleration and body forces in the ith spatial direction, respectively. The time derivatives are zero for our steady flow. Moreover, the density is constant since we study a low-speed flow. The term τ_{ij} is the Reynolds stress tensor that is defined as:

$$\tau_{ij} = \mu\left(\frac{\partial u_i}{\partial x_j} + \frac{\partial u_j}{\partial x_i}\right) - \frac{2}{3}\mu\left(\frac{\partial u_i}{\partial x_i}\right)\delta_{ij}, \quad (3)$$

where δ_{ij} is the Kronecker delta which equals 1 when i and j are the same; otherwise, it equals 0. From Eqs. (1)–(3), in the absence of the body forces and neglecting the effects of the gravity, the Reynolds averaged momentum equation can be derived as follows:

$$\frac{\partial}{\partial t}(\rho u_i) + \frac{\partial}{\partial x_j}(\rho u_i u_j) = -\frac{\partial P}{\partial x_i} + \frac{\partial}{\partial x_j}\left[\mu\left(\frac{\partial u_i}{\partial x_j} + \frac{\partial u_j}{\partial x_i}\right) - \frac{2}{3}\mu\left(\frac{\partial u_i}{\partial x_i}\right)\right] + \frac{\partial\left(\overline{u_i' u_j'}\right)}{\partial x_j}. \quad (4)$$

The term $\overline{u_i' u_j'}$, which is related to the turbulence, appears in the momentum equation and should be expressed using a suitable turbulence model [11].

2.2. Turbulence model

In this study, the k-ω-based Shear Stress Transport (SST) turbulence model with automatic wall functions (mixed formulation) developed by Menter is used. k represents the turbulence kinetic energy and ω is the turbulence-specific dissipation rate. The SST k-ω turbulence model uses a combination of k-ω and k-ε turbulence models using a blending function that is able to change the model from k-ω to k-ε when the distance from the wall increases. Thus, the SST k-ω turbulence model benefits from the high convergence rate of the k-ε high-Reynolds model away from the surface, besides the high accuracy of the k-ω model near the wall [11]. This two-equation model is the most appropriate RANS-based turbulence model for predicting flow separation [24]. Generally, the SST k-ω turbulence model can be formulated as follows [11,24]:

$$\frac{\partial(\rho k)}{\partial t} + \frac{\partial(\rho u_j k)}{\partial x_j} = P - \beta^* \rho \omega k + \frac{\partial}{\partial x_j}\left[(\mu + \sigma_k \eta_t)\frac{\partial k}{\partial x_j}\right], \quad (5)$$

$$\frac{\partial(\rho \omega)}{\partial t} + \frac{\partial(\rho u_j \omega)}{\partial x_j} = \frac{\lambda}{\upsilon_t}P - \beta^* \rho \omega^2 + \frac{\partial}{\partial x_j}\left[(\mu + \sigma_\omega \eta_t)\frac{\partial \omega}{\partial x_j}\right] + 2(1 - F_1)\frac{\rho \sigma_{\omega 2}}{\omega}\frac{\partial k}{\partial x_j}\frac{\partial \omega}{\partial x_j}, \quad (6)$$

$$P = \min\left\{\tau_{ij}\frac{\partial u_i}{\partial x_j}, 20\beta^* \rho \omega k\right\}, \quad (7)$$

$$\tau_{ij} = \eta_t\left(\frac{\partial u_i}{\partial x_j} + \frac{\partial u_i}{\partial x_i} - \frac{2}{3}\frac{\partial u_k}{\partial x_k}\delta_{ij}\right) - \frac{2}{3}\rho k \delta_{ij}, \quad (8)$$

where the turbulent eddy viscosity η_t is:

$$\eta_t = \frac{\rho a_1 k}{\max(a_1 \omega, \omega F_2)}. \quad (9)$$

The blending functions F_1 and F_2 are as follows:

$$F_1 = \tanh\left\{\left\{\min\left[\max\left(\frac{\sqrt{k}}{\beta^* \omega y}, \frac{500\upsilon}{y^2 \omega}\right), \frac{4\rho \sigma_{\omega 2} k}{CD_{k\omega} y^2}\right]\right\}^4\right\}, \quad (10)$$

$$F_2 = \tanh\left\{\left[\max\left(\frac{2\sqrt{k}}{\beta^* \omega y}, \frac{500\upsilon}{y^2 \omega}\right)\right]^2\right\}, \quad (11)$$

where y is the distance to the nearest wall and $CD_{k\omega}$ is:

$$CD_{k\omega} = \max\left(2\rho \sigma_{\omega 2}\frac{1}{\omega}\frac{\partial k}{\partial x_i}\frac{\partial \omega}{\partial x_i}, 10^{-10}\right). \quad (12)$$

Far enough from the wall, F_1 equals 0 and the model switches to the k-ε model. However, near the wall (inside the boundary layer), F_1 equals 1 and the model switches to the k-ω model. More details of the above equations can be found in [24].

2.3. Details of the utilized numerical algorithm

The flow field around the hollow duct is simulated as an axisymmetric flow using ANSYS-Fluent commercial software. For pressure-velocity coupling, a coupled solver is applied to solve the system of coupled equations in a steady pressure-based algorithm. The SST k-ω turbulence model described in the previous

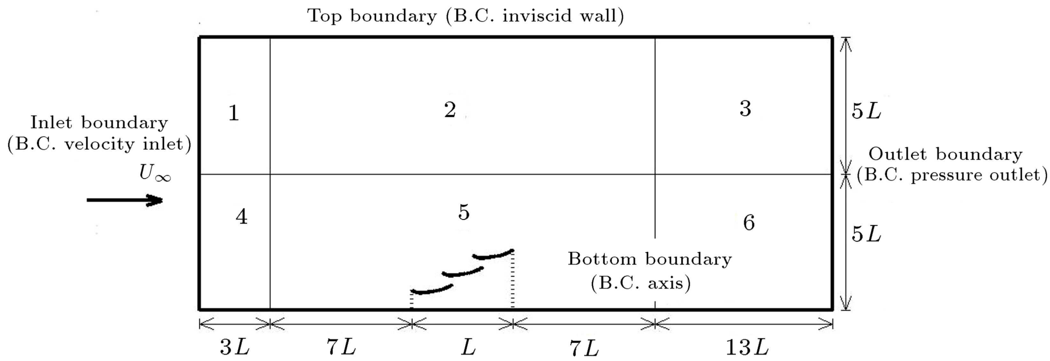

Figure 2. Computational domain and boundary conditions.

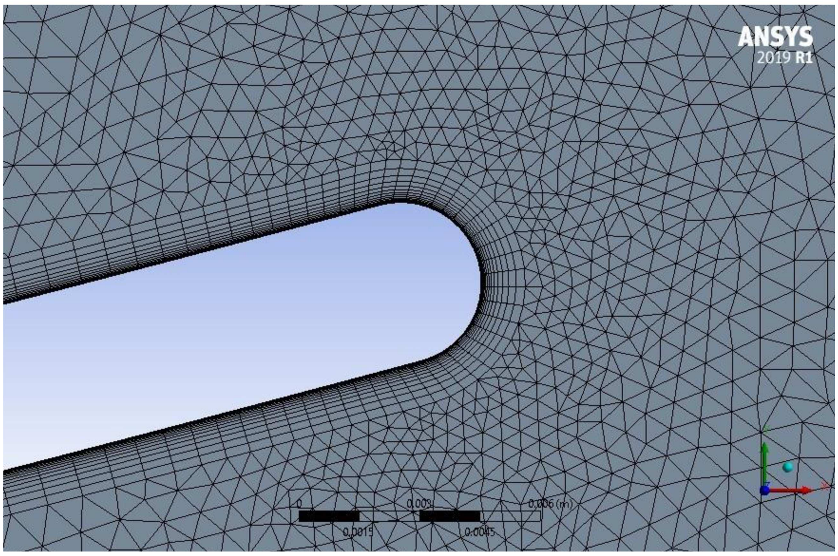

Figure 3. Mesh used in the part of the domain that contains the stages (zone 5 in Figure 2).

subsection is used to model flow turbulency. For spatial discretization, the least-squares cell-based method is used to compute the gradients and second-order accuracy is chosen for pressure interpolation. The highly accurate power-law scheme is utilized to calculate all the fluxes. The values of the residuals of continuity, momentum, turbulence kinetic energy, and specific turbulence dissipation rate were monitored to determine the convergence of the numerical method. Calculations stopped when all residuals were less than 10^{-6}. Selecting a double-precision option besides the mentioned high-accuracy schemes provided an accurate numerical simulation, which is in good agreement with the experimental results (Section 3). The computational domain containing 6 zones with the specified boundary conditions is shown in Figure 2.

2.4. Grid generation

As shown in Figure 2, the computational domain is divided up to 6 rectangular zones. A triangle non-structured mesh used for the part contains the bodies (zone 5) due to the high ability of triangular non-structured mesh in capturing the geometrical complexities of the model (Figure 3). In other parts of the domain (zones 1, 2, 3, 4, 6) that are far away from the bodies, a simple uniform orthogonal structured mesh is used due to its simplicity and high convergence rate. To satisfy the requirements of the SST k-ω turbulence model for acceptable ranges of the wall y^+, a suitable amount of the first-layer thickness in the boundary layer is modified from the former numerical experiences, and some trial and errors until the acceptable ranges of the wall y^+ are conducted. Diagrams of the average and maximum values of y^+ at all walls (all stage bodies) are illustrated in Figure 4. As can be seen in the diagrams, y^+ is in an acceptable range, which confirms the correctness of the chosen first-layer thickness.

Grids with different sizes are tested to find the suitable size of the grid. The mesh independency diagram is shown in Figure 5. As can be seen in the diagram, a grid with about 82000 cells is enough and then, the results are independent of the size of the grid.

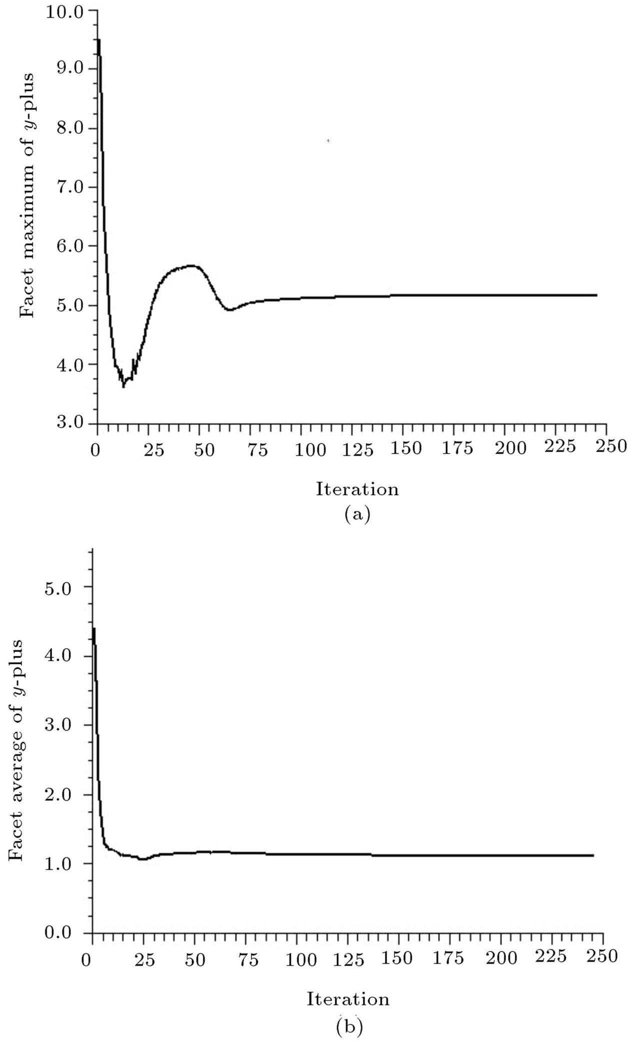

Figure 4. Amount of wall y^+: (a) Facet maximum of y^+ at all stages and (b) facet average of y^+ at all stages.

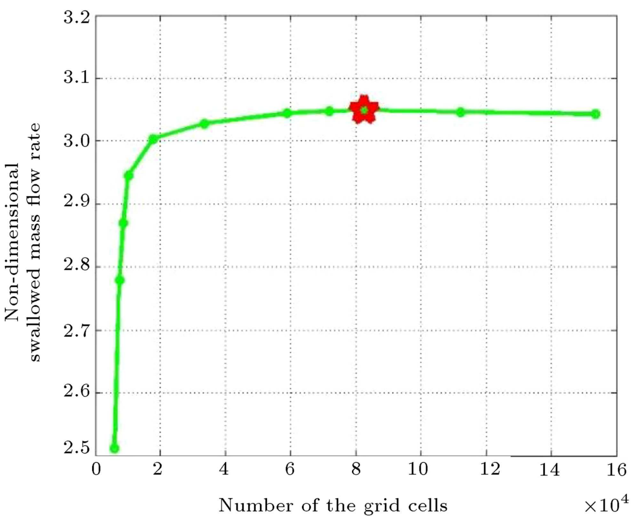

Figure 5. Grid independency diagram. Suitable size of the grid marked by star on the diagram. Non-dimensional swallowed mass flow rate defined by Eq. (5).

3. Validation of the CFD simulation

3.1. General description

Published experimental results of a hollow flanged duct tested in a wind tunnel at a velocity of 5 m/s performed by Ohya et al. [7] are used to validate the application of the numerical method in this study. The flow field around our case and the case they studied both contain a region of negative pressure at the inlet of the duct, a region of adverse pressure gradient inside the diffuser, and a large region of separation at the end of the duct.

3.2. Wind tunnel experiment

Ohya et al. [7] used the large boundary layer wind tunnel of the Research Institute for Applied Mechanics, Kyushu University to test various hollow-structure ducts. The wind tunnel had a measurement section that was 3.6 m wide ×2 m high ×15 m long and the maximum wind velocity was 30 m/s. The models were hung at the center of the wind tunnel section supported by strings. An I-type hot wire and a static pressure tube using a traversing system were employed to measure the distribution of the axial velocity u and the static pressure P along the axis line of the models. The model entrance diameter $D = 0.2$ m was the representative scale length of the model; the wind velocity was $U_\infty = 5$ m/s; and the Reynolds number was $Re = 6.8 \times 10^4$ [7].

3.3. Comparison of the numerical and experimental results

A schematic view of the duct tested in the wind tunnel is shown in Figure 6. In order to validate the numerical method used in this study, we model a hollow duct with a large flange ($h/D = 0.625$) and all of the other parameters are chosen exactly the same as those given in [7]. The axial velocity along the central axis line of the duct measured in the wind tunnel was employed to validate the viability of the numerical method applied in this study. Figure 7 shows the numerical results compared to the experimental results published in [7].

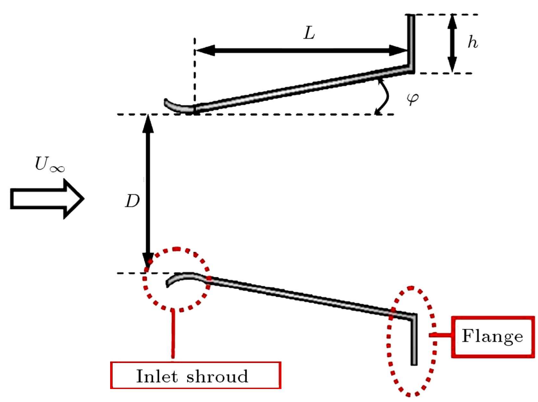

Figure 6. Schematic of the flanged duct tested in the wind tunnel in [7].

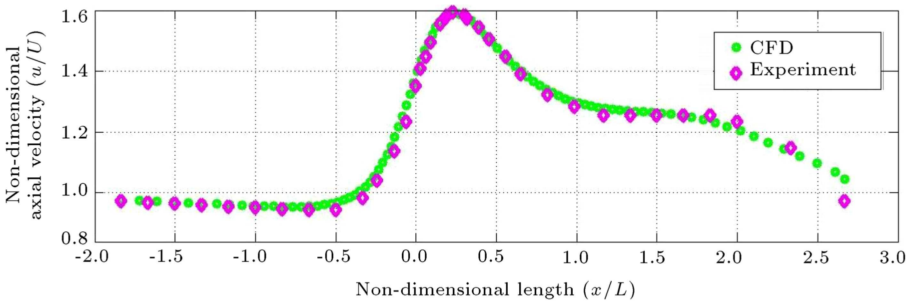

Figure 7. Validation diagram (experimental results from [7]).

x represents the axial distance from the throat in the direction of the flow, and L as shown in Figure 6 is the axial distance between the throat and the flange. u is the axial velocity at the position x on the central axis line of the duct and U is the wind tunnel velocity and equals 5 m/s. As can be seen in Figure 7, there is very good agreement between the numerical and experimental results.

4. Results and discussion

4.1. Introducing the parameters reported as results

In this part, some parameters that are used frequently in the result diagrams are introduced. The amount of the mass flow rate swallowed by a multi-stage duct is the main parameter to evaluate the performance of the duct. The profile of the axial velocity distribution versus the radial distance from the axis at the first-stage throat of a multi-stage duct, similar to what is shown in Figure 8, is used to compute the non-dimensional mass flow rate swallowed by the duct at the first-stage throat as follows:

$$NDSMFR = \frac{\int_{r=0}^{R_{throat}} \rho v_{axial(r)} (2\pi r) dr}{\rho \left(\pi R_{throat}^2\right) U_\infty}, \tag{13}$$

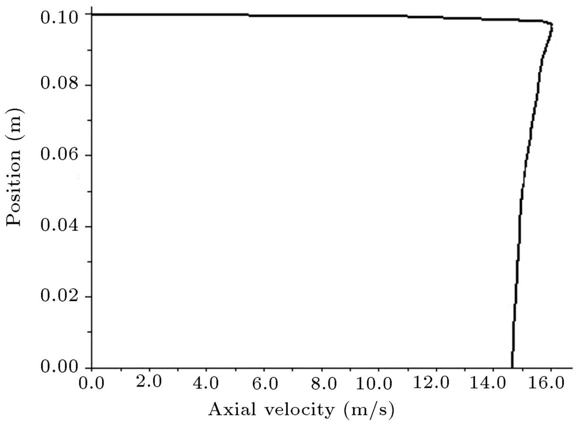

Figure 8. Profile of the axial velocity versus the radial position from the axis at the first-stage throat of a three-stage inducing duct at a wind velocity of 5 m/s.

where NDSMFR stands for the Non-Dimensional Swallowed Mass Flow Rate, and R_{throat} is the radius of the first-stage throat cross-section of the multi-stage duct. In addition, r is the radial distance from the duct axis on the first-stage throat cross-section plane, $v_{axial(r)}$ the axial velocity as a function of r, and U_∞ the free stream velocity.

Moreover, the average velocity at the first-stage throat of a multi-stage duct is computed as follows:

$$v_{average} = \frac{1}{A_{throat}} \int_{r=0}^{R_{throat}} v_{axial(r)} 2\pi r dr, \tag{14}$$

where A_{throat} is the area of the cross-section of the first-stage throat. Since we are discussing a hollow duct and there does not exist a turbine inside, the generated power is irrelevant. Instead, a new quantity called "swallowed power" is introduced to provide a criterion to evaluate the magnitude of the power augmentation caused by the duct. The swallowed power is the amount of the flow kinetic energy swallowed by the throat cross-section of the first stage of the duct computed as follows:

$$Swallowed\ power = \int_{r=0}^{R_{throat}} \left(\frac{1}{2}\rho v_{axial(r)}^3\right) 2\pi r dr. \tag{15}$$

To have a criterion to evaluate the computed values of power, the concept of "a duct with zero stages" is important and the power swallowed by the first-stage throat cross-section of such an imaginary duct is selected as the "reference power" as follows:

$$Reference\ power = \frac{1}{2}\rho \left(\pi R_{throat}^2\right) U_\infty^3. \tag{16}$$

The chosen reference power is the power swallowed on the same surface as the first-stage throat of a multi-stage duct if there is not any duct, and the mentioned surface is exposed to free stream. For the swallowed power to be independent of the geometrical sizes, the Non-Dimensional Swallowed Power (NDSP) is defined as follows:

$$NDSP = \frac{swallowed\ power}{reference\ power}$$

$$= \frac{\int_{r=0}^{R_{throat}} \left(\frac{1}{2}\rho v_{axial(r)}^3\right) 2\pi r dr}{\frac{1}{2}\rho \left(\pi R_{throat}^2\right) U_\infty^3}. \tag{17}$$

The values of the swallowed power and reference power are computed through Eqs. (15) and (16), respectively.

4.2. Single-stage duct analysis

4.2.1. General description

Since a multi-stage inducing duct consists of some converging-diverging ducts, called stages, studying the performance of a single converging-diverging duct is important. In this section, a single stage is studied and effect of its geometrical parameters is investigated. Figure 9 shows the velocity contour of the flow field around a single-stage duct. Details of the simulation are given in Tables 1, 2, and 3.

Schematic of a single-stage duct is shown in Figure 10. As can be seen in the figure, the longitudinal sections of the duct act like a system of airfoils whose lift forces neutralize each other due to the axisymmetric geometry of the duct. However, their generated circulations boost each other and generate a low-pressure region at the inlet of the duct. As can be seen in the contours, a low-pressure region is generated at the inlet of the duct and it swallows the flow inside the duct.

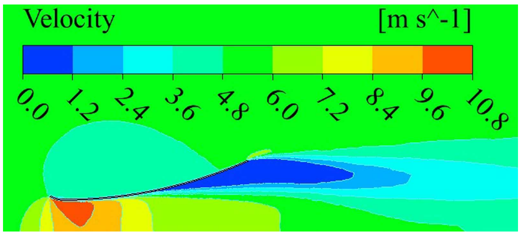

Figure 9. Flow field around a single-stage duct (contour of the velocity distribution).

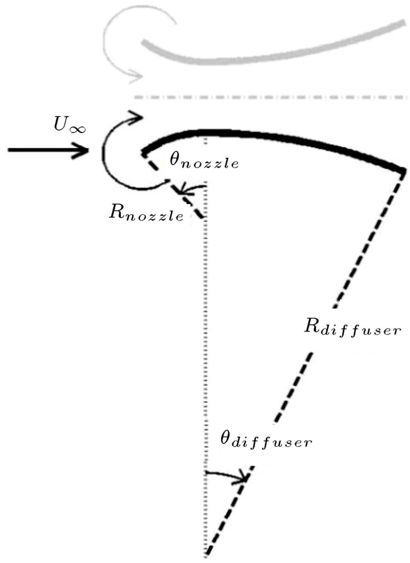

Figure 10. Schematic of a single-stage duct.

Table 1. Geometrical parameters of the reference case chosen for all single-stage numerical tests.

Parameter	Value
R_{throat}	0.1 m
Non-dimensional R_{nozzle} (R_{nozzle}/R_{throat})	0.75
θ_{nozzle}	30°
Non-dimensional $R_{diffuser}$ ($R_{diffuser}/R_{throat}$)	12.5
$\theta_{diffuser}$	24°

Table 2. Air properties chosen for all numerical simulations.

Parameter	Temperature (°C)	Density (kg/m^3)	Viscosity (kg/m.s)
Value	15	1.225	$1.7894 * 10^{-5}$

4.2.2. Test plan (for single-stage tests)

A single-stage duct with geometrical parameters expressed in Table 1 was chosen as the reference geometry. When the effect of each parameter is studied, all other parameters are fixed and equal to those in the reference case (Table 1). The reference case geometry should be as general as possible so that the effect of all parameters can be seen without being affected by unsuitable values assigned to other parameters. For example, we will not be able to observe the effect of $\theta_{diffuser}$ properly if the value assigned to $R_{diffuser}$ is too small.

Properties of the air and the free stream at which all performed numerical simulations (including single-stage, dual-stage, and multi-stage cases) are expressed in Tables 2 and 3, respectively.

4.2.3. Effect of nozzle angle (θ_{nozzle})

Effect of nozzle angle is studied in this part and the results are shown in Figure 11. All other geometrical

Table 3. Free stream properties.

Parameter	Axial velocity (m/s)	Radial velocity (m/s)	Turbulence intensity (%)	Turbulence viscosity ratio (%)
Value	5	0	5	10

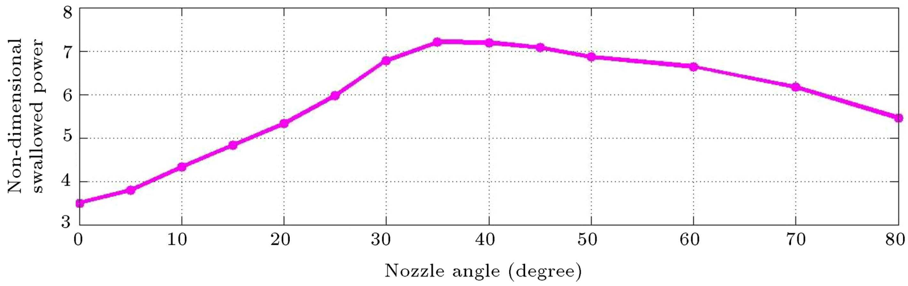

Figure 11. Effect of the nozzle angle (θ_{nozzle}) on the non-dimensional swallowed power.

parameters are fixed as in Table 1 and only the nozzle angle varies.

If we imagine the longitudinal section of the duct as an airfoil (Figure 10), when the nozzle angle increases, the camber of this airfoil will be increased, causing more circulation which in turn leads to greater suction and higher mass flow rate swallowed by the duct. However, as the angle of the nozzle rises, the blockage effect due to the larger cross-section of the nozzle is increased as well and it attempts to reduce the mass flow rate swallowed by the duct. When the nozzle angle is small, the blockage effect is small as well and the mentioned effect of the increase in the camber is the dominant factor and the swallowed flow increases as the nozzle angle increases. However, when the nozzle angle increases too much, the blockage effect rises and becomes the dominant factor. As can be seen in the diagram, further increase in the nozzle angle causes the swallowed flow to begin reducing.

4.2.4. Effect of nozzle radius (R_{nozzle})

Effect of nozzle radius is studied in this part and the results are shown in Figure 12. All other geometrical parameters are fixed as in Table 1 and only the nozzle radius varies.

Similar to the previous section, if the longitudinal profile of the duct is conceived as an airfoil (Figure 10), when the nozzle radius is small, increase in the nozzle radius results in increase in the camber of the airfoil, causing increase in the circulation and suction and, finally, increase in the mass flow rate swallowed by the duct. However, as the radius of the nozzle rises, the blockage effect due to the larger cross-section of the nozzle rises as well, facilitating the reduction of the swallowed flow by the duct. At first, the nozzle radius and the blockage effect caused by it are small and the mentioned growing effect due to increase in the nozzle radius is the dominant factor and the swallowed flow increases. However, with further increase in the nozzle radius, the blockage effect rises and becomes the dominant factor and the swallowed flow starts decreasing as the nozzle radius increases.

4.2.5. Effect of diffuser angle ($\theta_{diffuser}$)

In this section, effect of the diffuser angle ($\theta_{diffuser}$) is studied and the results are shown in Figure 13. All other geometrical parameters are fixed as in Table 1 and only the diffuser angle varies.

When the angle of the diffuser starts increasing from zero, the camber of the airfoil (longitudinal section of the duct shown in Figure 10) begins increasing as well, leading to increase in the circulation and suction and finally increase in the swallowed flow by the duct. With further increase in the diffuser angle, separation occurs and creates a low-pressure region at the outlet of the duct, which causes the swallowed mass diagram to continue increasing. However, with further increase in the diffuser angle, the separated region spreads too much, which results in a decrease in the swallowed flow.

4.2.6. Effect of diffuser radius ($R_{diffuser}$)

Effect of diffuser radius ($R_{diffuser}$) is studied in this part and the results are shown in Figure 14. All other geometrical parameters are fixed as in Table 1 and only the diffuser radius varies.

As the diffuser radius starts increasing from zero, the generated circulation of the airfoil (longitudinal sec-

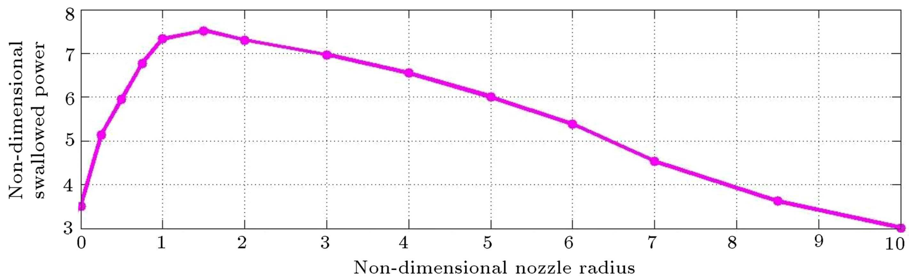

Figure 12. Effect of the non-dimensional nozzle radius (R_{nozzle}/R_{throat}) on the non-dimensional swallowed power.

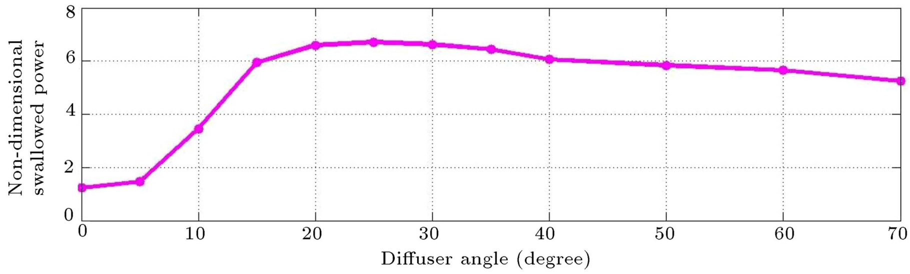

Figure 13. Effect of the diffuser angle ($\theta_{diffuser}$) on the non-dimensional swallowed power.

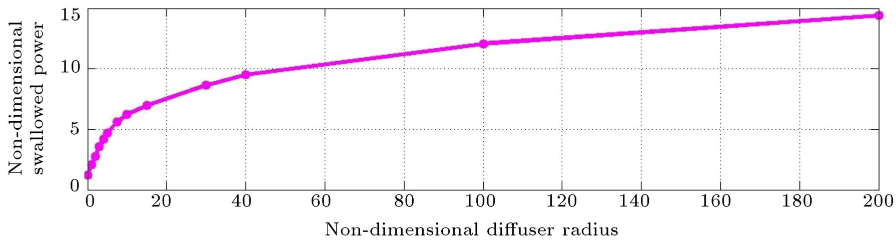

Figure 14. Effect of the non-dimensional diffuser radius ($R_{diffuser}/R_{throat}$) on the non-dimensional swallowed power.

tion of the duct shown in Figure 10) begins increasing, which results in increase in the swallowed flow. With further increase in the diffuser radius, the separation occurs and low pressure in the separated region at the outlet causes the swallowed flow diagram to continue increasing. However, the larger the diffuser radius, the lower the body curvature of the diffuser. As the diffuser angle rises, the flow senses a smaller adverse pressure gradient, which postpones the separation and yields increase in the swallowed flow. Although the spread of the separated region has a decreasing effect on the swallowed flow, the growing effect due to the separation postponement is dominant and the diagram continues its increasing trend. When the diffuser radius increases too much, the diffuser body becomes like a simple cone and the sensitivity of the adverse gradient to the body curvature decreases. Considering the diffuser longitudinal section as an arc of a circle, use of a simple geometrical analysis can illustrate the following:

$$\lim_{R_{diffuser}\to\infty}\left[\frac{\partial}{\partial R_{diffuser}}\left(\frac{\partial A_{diffuser(x)}}{\partial x}\right)\right]=0, \quad (18)$$

where x is the axial distance from the throat cross-section in the direction of the free stream flow, $R_{diffuser}$ the curvature radius of the diffuser body, and $A_{diffuser(x)}$ the area of diffuser cross-section at distance x from the throat. As can be seen in Figure 14, the sensitivity to the diffuser radius goes to zero as the diffuser radius rises to infinity.

4.2.7. Comparing the influence of the geometrical parameters of a single-stage duct on the duct performance

In this section, the potential impact of the four discussed affecting geometrical parameters of a single-stage duct on the duct performance is studied. The range of changes in the independent, affecting geometrical parameters as well as the range of the corresponding changes in the swallowed power are given in Table 4. Figure 15 shows the potential impact of the four mentioned parameters using the assigned indices 1 to 4. The value of the NDSP related to the reference duct (Table 1) is selected as the reference to calculate the relative augmentation percentages in Table 4 and Figure 15. As can be seen in Figure 15, the range of the changes in duct performance due to changing the diffuser parameters is wider than that of the changes caused by changing the nozzle parameters. Moreover,

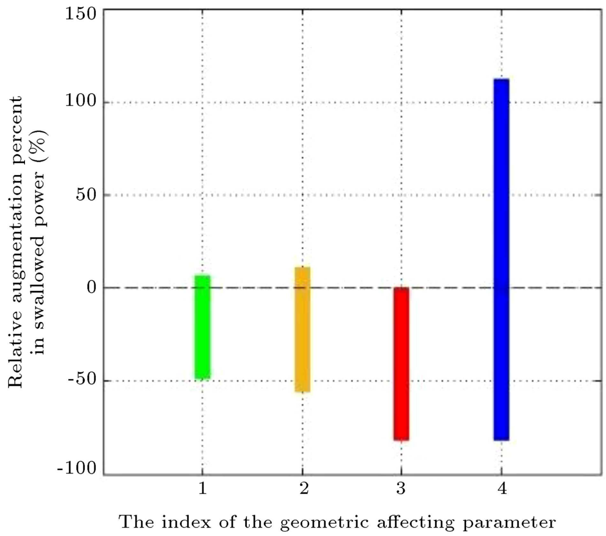

Figure 15. A comparison between the potential impact of the four geometrical affecting parameters of a single-stage duct. Indices 1 to 4 are assigned to the affecting parameters in Table 4.

Table 4. List of the geometrical affecting parameters of a single-stage duct, the specified indices, and the ranges of the changes.

$\text{parameter}_{\text{index}}$	Description	The range of the changes	The range of the corresponding changes in relative swallowed power (%)
P_1	θ_{nozzle}	0°–80°	[−48.4, 6.3]
P_2	Non-dimensional R_{nozzle} (R_{nozzle}/R_{throat})	0–10	[−55.6, 10.8]
P_3	$\theta_{diffuser}$	0°–70°	[−81.8, 0.0]
P_4	Non-dimensional $R_{diffuser}$ ($R_{diffuser}/R_{throat}$)	0–200	[−81.8, 112.0]

the range of the changes in duct performance caused by changing the angle is smaller than that of the changes caused by radius variation.

4.3. Dual-stage inducing duct analysis

4.3.1. General description

In this part, ducts with two stages are studied. Figure 16 shows the pressure contour of the flow field around a dual-stage duct. All details of the simulation are given in Tables 2, 3, 5.

4.3.2. Test plan (for dual-stage tests)

Studying the effect of adding the second stage and the relative locations of the stages is the purpose of this part. Values given to geometrical parameters of both stages are fixed that are the same as those dedicated in the previous section (Table 1). A dual-stage duct with a certain geometry is selected as the reference case for all simulations of dual-stage ducts in this part (Table 5).

4.3.3. Effect of radial gap

The effect of the radial gap between two stages is studied in this part and the results are shown in Figure 17. All other geometrical parameters are fixed as in the reference case and only the radial gap varies. As shown in Figure 16, overlapping stages create a converging channel between the stages that causes the flow to accelerate in passing the radial gap between the stages. When the radial gap is too small, the

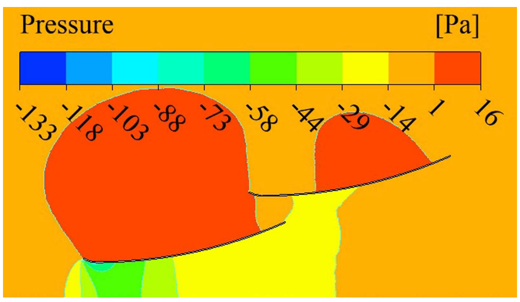

Figure 16. Flow field around a dual-stage duct (contour of the pressure distribution).

Table 5. Geometrical parameters of the reference case chosen for all dual-stage tests. The value of 0.713 for *non-dimensional radial gap*$_{stages\ 1-2}$ refers to the state at which the *radial gap*$_{stages\ 1-2}$ is half the first-stage diffuser outlet radius.

$R_{throat,stage\ 1}$ (the reference length)	0.1 m
Non-dimensional $R_{nozzle,stage\ 1}$ ($R_{nozzle,stage\ 1}/R_{throat,stage\ 1}$)	0.75
$\theta_{nozzle,stage\ 1}$	30°
Non-dimensional $R_{diffuser,stage\ 1}$ ($R_{diffuser,stage\ 1}/R_{throat,stage\ 1}$)	12.5
$\theta_{diffuser,stage\ 1}$	24°
Non-dimensional radial gap$_{stages\ 1-2}$ (radial gap$_{stages\ 1-2}/R_{throat,stage+1}$)	0.713
Non-dimensional overlapping length$_{stages\ 1-2}$ (overlapping length$_{stages\ 1-2}/R_{throat,stage\ 1}$)	1.0
Non-dimensional $R_{nozzle,stage\ 2}$ ($R_{nozzle,stage\ 2}/R_{throat,stage\ 1}$)	0.75
$\theta_{nozzle,stage\ 2}$	30°
Non-dimensional $R_{diffuser,stage\ 2}$ ($R_{diffuser,stage\ 2}/R_{throat,stage\ 1}$)	12.5
$\theta_{diffuser,stage\ 2}$	24°

blockage effect causes a decrease in the suction. As the radial gap grows, the blockage effect is weakened and the suction increases. However, massive increase in the radial gap causes the converging coefficient of the channel between the stages to decrease substantially, resulting in a decrease in the created suction.

4.3.4. Effect of the overlapping length

The effect of overlapping length between two stages is studied in this part and the results are shown in Figure 18. When the overlapping length increases from negative to positive amounts, as shown in Figure 16, overlapping stages create a converging channel between the stages. Due to the specific shape of the stages, an increase in overlapping length results in an increase in the geometrical converging coefficient of the created

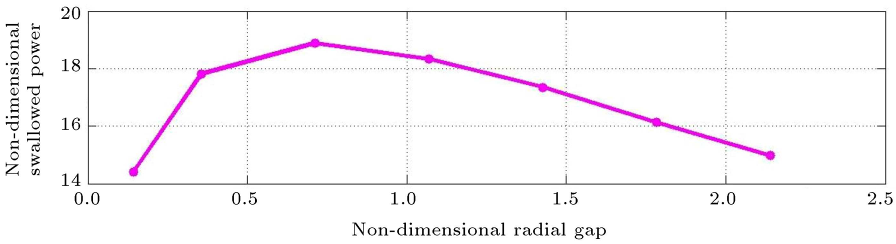

Figure 17. Effect of the *non-dimensional radial gap*$_{stages\ 1-2}$ (*radial gap*$_{stages\ 1-2}/R_{throat,stage\ 1}$) on the non-dimensional swallowed power.

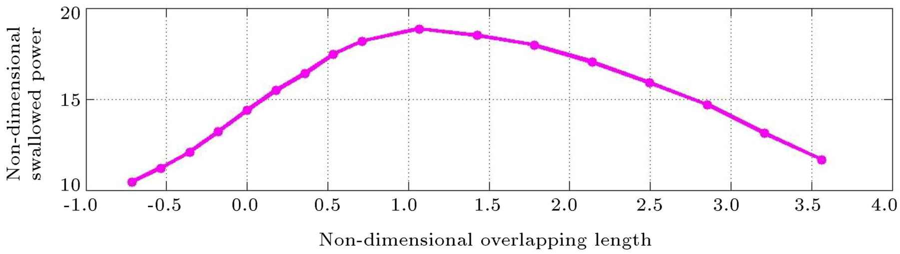

Figure 18. Effect of the *non-dimensional overlapping length*$_{stages\ 1-2}$ (*overlapping length*$_{stages\ 1-2}/R_{throat,stage\ 1}$) on the non-dimensional swallowed power.

gap channel between the stages. At first, the positive overlapping length is small and the geometrical converging ratio of the gap channel is not too large to cause a blockage in the flow field, increase in overlapping length causes an increase in the suction. However, with further increase in the overlapping length, the blockage effect occurs which results in a decrease in the suction.

4.3.5. Comparison of the impact of the geometrical parameters related to the consecutive stages in a dual-stage duct on the duct performance

Figure 19 shows the potential impact of the parameters mentioned in Table 6. The value of the swallowed power related to the reference dual-stage duct (Table 5) is chosen as the reference to calculate the relative augmentation percentages in Figure 19. Since the radial gap and overlapping length are geometrical parameters that depend on the geometry of both stages, there is no set rule to determine which of the two parameters is more effective. Depending on the geometry of the two consecutive stages, one or another parameter may be more effective.

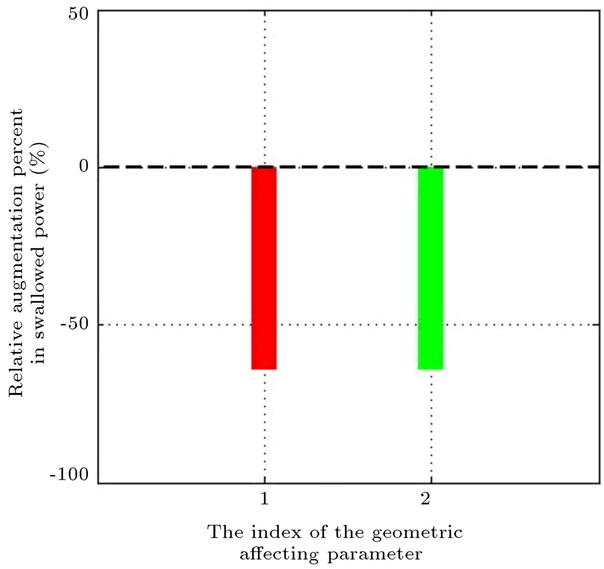

Figure 19. A comparison between the potential impact range of the geometrical affecting parameters related to the consecutive stages in a dual-stage duct. Indices 1 and 2 are assigned to the affecting parameters in Table 6.

Table 6. List of the geometrical affecting parameters related to the consecutive stages in a dual-stage duct, the assigned indices, and the ranges of the changes.

Parameter$_{\text{index}}$	**Description**	**The range of the changes**	**The range of the corresponding changes in the swallowed power (%)**
P_1	Non-dimensional radial gap$_{stages\ 1-2}$ (radial gap$_{stages\ 1-2}/R_{throat,stage\ 1}$)	$[0.1426,\ \infty)$	$[-64.1,\ 0.0]$
P_2	Non-dimensional overlapping length$_{stages\ 1-2}$ (overlapping length$_{stages\ 1-2}/R_{throat,stage\ 1}$)	$[-0.713,\ \infty)$	$[-64.0,\ 0.0]$

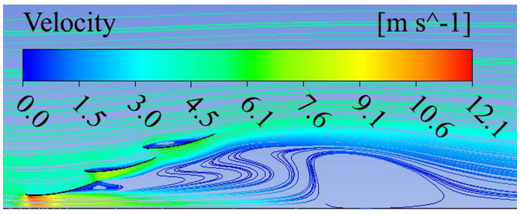

Figure 20. Flow field around a multi-stage (three-stage) duct (streamlines).

4.4. Multi-stage analysis

4.4.1. General description

In this part, ducts with several stages are investigated. Figure 20 shows the streamlines of the flow field around a three-stage duct. As can be seen in Figure 20, inducing effect due to the addition of the third stage causes an increase in the first stage velocity compared to a dual-stage duct.

4.4.2. Test plan (for multi-stage tests)

In this section, various multi-stage ducts with the number of stages from 1 to 24 are simulated. Since we intend to study the effect of the number of the stages, longitudinal sections of all stages are chosen to be the same for simplicity. Also, the radial gaps and the overlapping lengths between all of the stages are chosen to be the same, as well (Table 5).

4.4.3. Effect of the number of the stages

In this part, multi-stage ducts up to 24 stages are simulated and the results are shown in Figure 21. As can be seen in Figure 21, as the number of the stages increases, the slope of the diagram decreases. It is shown that the first stages are more effective than the last ones. In fact, the later downstream stages need their previous stages as intermediates to be able to affect the mass flow rate swallowed by the first stage. Obviously, the larger the number of the intermediate stages, the lower the inducing effect on the first stage.

4.4.4. Effect of the wind velocity on the performance of the multi-stage inducing ducts

Figure 22 shows the average axial velocity at the first-stage throat of the ducts with various stages at various wind velocities. Except for velocity that varies in this section, all other properties of the free stream are the same as those given in Table 3. As can be seen in Figure 22, when the number of the stages is very small, the diagrams are obviously steep and when the number of the stages increases to larger numbers, the slope of the diagrams approaches zero. In other words, as mentioned in the previous section, the first stages are more effective than the last ones. However, as shown in Figure 22, diagrams of different wind velocities exhibit different behaviors. The diagrams' slope is larger at higher wind velocities than lower wind velocities. According to the ducts with one or two stages, as the number of the stages increases, the slope of the diagrams at higher wind velocities approaching zero is slower than that at lower velocities. At higher wind speeds, the inducing suction effect is stronger and it, therefore, causes a stronger increase in the swallowed mass flow rate at the first-stage throat. In other words, the performance of a multi-stage inducing duct is enhanced at higher free stream velocities.

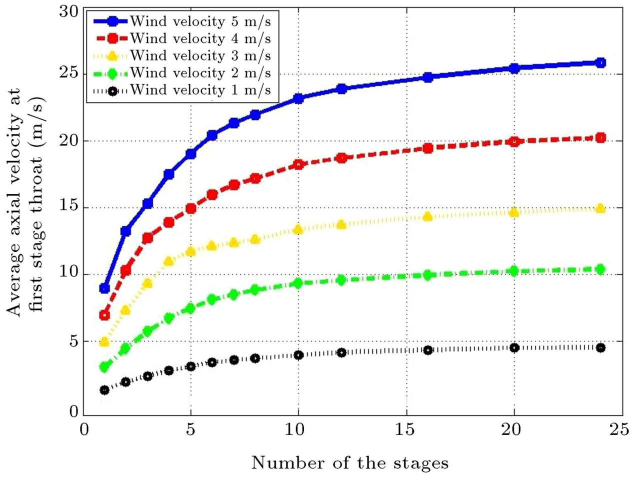

Figure 22. Effect of the number of stages on the performance of a multi-stage inducing duct at various wind velocities.

The Absolute Augmentation Percentage in Swallowed Power ($\mathrm{AAP_{SP}}$) is defined as follows:

$$AAP_{SP}=\frac{swallowed\ power-reference\ power}{reference\ power}\times 100\%, \tag{19}$$

where the swallowed power and the reference power are computed using Eqs. (15) and (16), respectively.

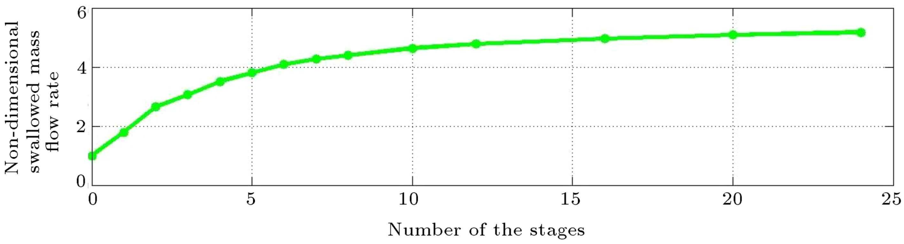

Figure 21. Effect of the number of the stages on the non-dimensional swallowed mass flow rate.

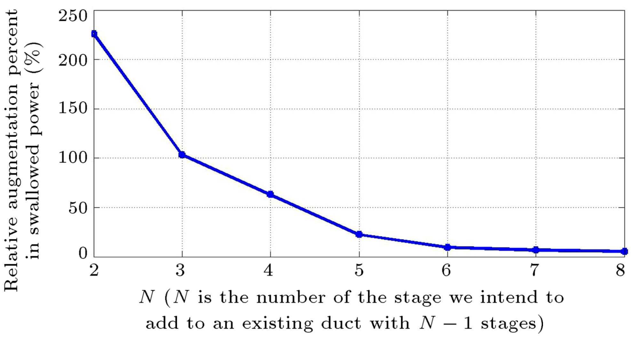

Figure 23. Diagram of the relative effectiveness of adding the Nth stage to an existing duct with $(N-1)$ stages defined by Eq. (20).

4.4.5. Determining the number of the stages of a multi-stage inducing duct

In contrast to the absolute augmentation percentage in swallowed power, the Relative Augmentation Percentage in Swallowed Power ($\mathrm{RAP_{SP}}$) is defined as follows:

$$RAP_{SP} = \frac{SP_N - SP_{N-1}}{SP_{N-1}} \times 100\%, \tag{20}$$

where SP_N is the swallowed power after adding the Nth stage, SP_{N-1} is the swallowed power before adding the Nth stage, and values of swallowed powers (SP_N and SP_{N-1}) are computed from Eq. (15). Figure 23 shows the diagram of the relative augmentation percentage in swallowed power as the number of the stages increases from $N-1$ to N. As can be seen in Figure 23, as N grows, the relative effectiveness of adding the Nth stage to the existing duct with $N-1$ stages decreases continuously, whereas the absolute effectiveness of the new-added stage (Nth stage), as Figure 22 shows, increases continuously. On the other hand, the last stages are larger, heavier, and further away from the turbine; therefore, the costs of manufacturing the stages and building the necessary equipment for structural support significantly increase at the last stages. According to the absolute diagrams seen in Figure 21 and Figure 22, although the larger the number of the stages, the greater the swallowed power, the relative diagram illustrated in Figure 23 along with some economic considerations on the costs of manufacturing the stages and building the needed equipment for structural support help determine the number of the stages. In most applications, choosing two, three, or four stages is enough to achieve an acceptable result while it is not economical to use more stages.

5. Conclusion

In this study, a specific configuration of the duct, called Multi-Stage Inducing Duct, was presented and numerically simulated, and effects of its geometrical parameters were investigated. It was shown that using a multi-stage inducing duct would lead to a significant increase in the wind velocity profile. In a multi-stage inducing duct, the downstream stages induce a suction effect on the upstream stages. The effect of the geometrical parameters of a single-stage duct was investigated and it was concluded that the parameters of the diffuser part would be more effective than the parameters of the nozzle part. Moreover, it was observed that the range of changes in the swallowed power caused by the changes in the radius was wider than the range of the changes caused by the changes in the angle in both nozzle and diffuser parts. When the second stage was added, the inducing effect occurred and the suction produced by the second stage helped the flow to exit easier from the first-stage outlet; consequently, the greater mass flow rate was swallowed by the first stage. The effects of changes in the radial gap and overlapping length between two consecutive stages on inducing effect were studied separately and it was shown that increase in the radial gap between two consecutive stages increases and decreases the induced suction, orderly, at the first-stage throat. Similar behavior was observed when the overlapping length between two consecutive stages increased. Comparison of the impacts of the radial gap and overlapping length illustrated that they were of the same power of influence and none was negligible compared to the other. Effects of the number of the stages and the free stream velocity on the duct performance were studied together and it was shown that the last stages were less effective than the first ones due to their higher distance from the first-stage throat. It was shown that the strength of the inducing effect depended on the free stream velocity and the higher the free stream velocity, the greater the effectiveness of the downstream stages. Finally, the effectiveness of adding a new stage to an existing multi-stage inducing duct was studied from two different points of view: absolute effectiveness and relative effectiveness. It was shown that although the higher the number of the stages, the greater the swallowed power from an absolute point of view; however, from a relative point of view, it is not usually economical to use more than three or four stages due to the high costs of manufacturing and building the equipment needed for structural support.

Abbreviations

NDSMFR	Non-Dimensional Swallowed Mass Flow Rate
$\mathrm{AAP_{SP}}$	Absolute Augmentation Percentage in Swallowed Power
$\mathrm{RAP_{SP}}$	Relative Augmentation Percentage in Swallowed Power
SP_N	Swallowed Power by a N-stage duct (after the Nth stage be added)

SP_{N-1}	Swallowed Power by a $(N-1)$-stage duct (before the Nth stage be added)

Nomenclature

ρ	Fluid density
P	Static pressure
g_i	Component of the gravitational acceleration in the ith spatial direction
t	Time
δ_{ij}	Kronecker delta
F_i	Component of the body force in the ith spatial direction
τ_{ij}	Reynolds stress tensor
u_i	Component of the velocity in the ith spatial direction
x_i	Component of the length in the ith spatial direction
μ	Fluid viscosity
u'_i	Turbulent velocity fluctuation in the ith spatial direction
k	Turbulence kinetic energy
ω	Turbulence specific dissipation rate
U_∞	Free stream velocity
r	Radial distance from the duct axis at the first stage throat plane
$V_{axial\ (r)}$	Axial velocity as a function of r
x	Axial distance from the throat cross section in the direction of the free stream flow
R_{throat}	Radius of the first stage throat cross section
A_t	Area of the first stage throat cross section
θ_{nozzle}	Arc angle of the nozzle body
$\theta_{diffuser}$	Arc angle of the diffuser body
R_{nozzle}	Curvature radius of the nozzle body
$R_{diffuser}$	Curvature radius of the diffuser body
$A_{diffuser(x)}$	Area of diffuser cross section at the distance x from the throat

References

1. Tahani, M., Babayan, N., Mehrnia, S.M., et al. "A novel heuristic method for optimization of straight blade vertical axis wind turbine", *Energy Conversion and Management*, **127**, pp. 461–476 (2016).
2. Tahani, M., Rabbani, A., Kasaeian, A., et al. "Design and numerical investigation of Savonius wind turbine with discharge flow directing capability", *Energy*, **130**, pp. 327–338 (2017).
3. Tahani, M., Maeda, T., Babayan, N., et al. "Investigating the effect of geometrical parameters of an optimized wind turbine blade in turbulent flow", *Energy Conversion and Management*, **153**, pp. 71–82 (2017).
4. Tahani, M., Kavari, G., Masdari, M., et al. "Aerodynamic design of horizontal axis wind turbine with innovative local linearization of chord and twist distributions", *Energy*, **131**, pp. 78–91 (2017).
5. Tahani, M., Babayan, N., and Pouyaei, A. "Optimization of PV/Wind/Battery stand-alone system, using hybrid FPA/SA algorithm and CFD simulation, case study: Tehran", *Energy Conversion and Management*, **106**, pp. 644–659 (2015).
6. Abe, K., Nishida, M., Sakurai, A., et al. "Experimental and numerical investigations of flow fields behind a small wind turbine with a flanged diffuser", *Wind Engineering*, **93**(12), pp. 951–970 (2005).
7. Ohya, Y., Karasudani, T., Sakurai, A., et al. "Development of a shrouded wind turbine with a flanged diffuser", *J. of Wind Engineering and Industrial Aerodynamics*, **96**, pp. 524–539 (2008).
8. Kosasih, B. and Tondelli, A. "Experimental study of shrouded micro-wind turbine", *Procedia Engineering*, **49**, pp. 92–98 (2012).
9. Jafari, S. and Kosasih, B. "Flow analysis of shrouded small wind turbine with a simple frustum diffuser with computational fluid dynamics simulations", *Wind Engineering and Industrial Aerodynamics*, **125**, pp. 102–110 (2014).
10. Mansour, K. and Meskinkhoda, P. "Computational analysis of flow fields around flanged diffusers", *Wind Engineering and Industrial Aerodynamics*, **124**, pp. 109–120 (2014).
11. Zabihzade, S., Alimirzazadeh, S., and Rad, M. "RANS simulations of the stepped duct effect on the performance of ducted wind turbine", *Wind Engineering and Industrial Aerodynamics*, **145**, pp. 270–279 (2015).
12. Han, W., Yan, P., Han, W., et al. "Design of wind turbines with shroud and lobed ejectors for efficient utilization of low-grade wind energy", *Energy*, **89**, pp. 687–701 (2015).
13. Al-Sulaiman, F. "Exergoeconomic analysis of ejector-augmented shrouded wind turbines", *Energy*, **128**, pp. 264–270 (2017).
14. Khamlaj, T.A. and Rumpfkeil, M.P. "Analysis and optimization of ducted wind turbines", *Energy*, **162**, pp. 1234–1252 (2018).
15. Saleem, A. and Kim, M. "Effect of rotor tip clearance on the aerodynamic performance of an aerofoil-based ducted wind turbine", *Energy Conversion and Management*, **201**, pp. 1–14 (2019).
16. Noorollahi, Y., Ghanbari, S., and Tahani, M. "Numerical analysis of a small ducted wind turbine for performance improvement", *Int. J. of Sustainable Energy*, **39**(3), pp. 290–307 (2020).
17. Keramat, N., Najafi, G., Tavakkoli, T., et al. "An innovative variable shroud for micro wind turbines", *Renewable Energy*, **145**, pp. 1061–1072 (2020).
18. Bontempo, R. and Manna, M. "Diffuser augmented

wind turbines: Review and assessment of theoretical models", *Applied Energy*, **280**, pp. 1–17 (2020).

19. Keramat, N., Najafi, G., Tavakkoli, T., et al. "Mathematical modeling of a horizontal axis shrouded wind turbine", *Renewable Energy*, **146**, pp. 856–866 (2020).
20. Prasad, K.R., Kumar, V.M., Swaminathan, G., et al. "Computational investigation and design optimization of a duct augmented wind turbine (DAWT)", *Mater. Todays: Proceedings*, **22**(3), pp. 1186–1191 (2020).
21. Rivarolo, M., Freda, A., and Traverso, A. "Test campaign and application of a small-scale ducted wind turbine with analysis of yaw angle influence", *Applied Energy*, **279**, pp. 1–9 (2020).
22. Avallone, F., Ragni, D., and Casalino, D. "On the effect of the tip-clearance ratio on the aeroacoustics of a diffuser-augmented wind turbine", *Renewable Energy*, **152**, pp. 1317–1327 (2020).
23. Nardecchia, F., Groppi, D., Garcia, D.A., et al. "A new concept for a mini ducted wind turbine system", *Renewable Energy*, **175**, pp. 610–624 (2021).
24. Menter, F.R., Kuntz, M., and Langtry, R. "Ten years of industrial experience with the SST turbulence model", *Turbulence, Heat and Mass Transfer*, **4**, pp. 625–632 (2003).

Biographies

Mojtaba Tahani is an Associate Professor at the Faculty of New Sciences and Technologies (FNST), University of Tehran, Amiraabad Shomali, Tehran, Iran. He obtained his PhD at Iran University of Science and Technology. His fields of research are CFD, turbulence flows, aerodynamics, fluid mechanics, and thermodynamics.

Mehran Masdari is an Assistant Professor at University of Tehran. He is holding BSc Eng, MSc, and PhD degrees in Aerodynamics from Sharif University of Technology. He published more than 50 scientific papers in English and Persian. He has 15 years of job experience both in industry and academic fields. Various aerospace courses and student projects were conducted by him. His research interests transitional flows, applied aerodynamics, experimental fluid dynamics, Particle Image Velocimetry (PIV), bluff body wakes, turbulent boundary layer, wind engineering, mechanical engineering, fluid mechanics, aerodynamics, turbomachinery, turbulence, wind turbine, Vertical Axis Wind Turbine (VAWT), micro air vehicles, fluid mechanics, aerospace engineering, fluid dynamics, wind tunnel testing, neural network, and data processing.

Amin Habibi is a PhD candidate in Aerospace Engineering (aerodynamics) at the Faculty of New Sciences and Technologies, University of Tehran, Tehran, Iran. His main research direction is wind engineering and computational fluid dynamics.

Mojtaba Mirhosseini graduated with a PhD in Energy Engineering from Aalborg University, Denmark. Now, he is an Assistant Professor in School of Advanced Technologies at Iran University of Science and Technology (IUST), Tehran, Iran. His research focuses on energy systems engineering and renewable energy technologies. One of his research interests and specialties is aerodynamics of wind turbines.